

# Stringent limits on the masses of the supermassive black holes in seven nearby galaxies \*

I. Pagotto<sup>1, \*\*</sup>, E.M. Corsini<sup>1, 2</sup>, E. Dalla Bontà<sup>1, 2</sup>, A. Beifiori<sup>3, 4</sup>, L. Costantin<sup>1</sup>, V. Cuomo<sup>1</sup>, L. Morelli<sup>1, 2</sup>, A. Pizzella<sup>1, 2</sup>, and M. Sarzi<sup>5</sup>

<sup>1</sup> Dipartimento di Fisica e Astronomia “G. Galilei”, Università di Padova, vicolo dell’Osservatorio 3, I-35122 Padova, Italy

<sup>2</sup> INAF-Osservatorio Astronomico di Padova, vicolo dell’Osservatorio 2, I-35122 Padova, Italy

<sup>3</sup> Universitäts-Sternwarte München, Scheinerstraße 1, D-81679 München, Germany

<sup>4</sup> Max-Planck-Institut für extraterrestrische Physik, Giessenbachstraße, D-85748 Garching bei München, Germany

<sup>5</sup> Centre for Astrophysics Research, University of Hertfordshire, College Lane, Hatfield AL10 9AB, UK

Received XXXX, accepted XXXX

Published online XXXX

**Key words** black hole physics – galaxies: kinematics and dynamics – galaxies: nuclei – galaxies: photometry

We present new stringent limits on the mass  $M_\bullet$  of the central supermassive black hole for a sample of 7 nearby galaxies. Our  $M_\bullet$  estimates are based on the dynamical modeling of the central width of the nebular emission lines measured over subarcsecond apertures with the Hubble Space Telescope. The central stellar velocity dispersion  $\sigma_c$  of the sample galaxies is derived from new long-slit spectra from ground-based observations and the bulge effective radius is obtained from a two-dimensional photometric decomposition of the  $i$ -band images from the Sloan Digital Sky Survey. The derived stringent  $M_\bullet$  limits run parallel and above the  $M_\bullet - \sigma_c$  relation with no systematic trend depending on the galaxy distance or morphology. This gives further support to previous findings suggesting that the nuclear gravitational potential is remarkably well traced by the width of the nebular lines when the gas is centrally peaked. With our investigation, the number of galaxies with stringent  $M_\bullet$  limits obtained from nebular-line width increases to 114 and can be used for studying the scaling relations between  $M_\bullet$  and properties of their host galaxies.

Copyright line will be provided by the publisher

## 1 Introduction

Over nearly three decades of measurements for the mass  $M_\bullet$  of central supermassive black holes (SBHs) have led to the conclusion that such objects should be nearly always present at the center of elliptical galaxies and bulges of disk galaxies (see Kormendy & Ho 2013, for a review). Furthermore, the finding that  $M_\bullet$  correlates with several properties of their host galaxies, and in particular with the velocity dispersion  $\sigma_\star$  of their spheroidal component (Gebhardt et al. 2000; Ferrarese & Merritt 2000), suggests that somehow SBHs and spheroids grew together (see Saglia et al. 2016). These mutual relationships between the black holes and their host galaxies could come from feedback mechanisms (see Silk & Rees 1998; Fabian 1999). Large  $M_\bullet$  samples across different morphological types are needed to fully understand the underlying process behind the  $M_\bullet - \sigma_\star$  relation, as clues may be present not only in the slope of this relation but also in its scatter, the behavior of outliers, and

secondary trends related for instance to galaxy morphology (Beifiori et al. 2012; McConnell & Ma 2013; Shankar et al. 2016).

For this purpose Beifiori et al. (2009, 2012) used archival Hubble Space Telescope (HST) spectroscopic data obtained with the Space Telescope Imaging Spectrograph (STIS) to estimate stringent limits on  $M_\bullet$  for 107 galaxies of various Hubble types, following the approach of Sarzi et al. (2002) to model the velocity dispersion of ionized-gas emission observed at sub-arcsecond scales. The sample of Beifiori et al. (2009) included an additional 21 objects with STIS data, but those were excluded since they missed a ground-based  $\sigma_\star$  measurement and thus could not be placed on the  $M_\bullet - \sigma_\star$  relation. In this paper, we aim at increasing the sample of galaxies with stringent  $M_\bullet$  limits, by selecting 7 Northern galaxies ( $\text{Dec (J2000.0)} > -10^\circ$ ) with detected emission lines in STIS spectra from the objects excluded by Beifiori et al. (2009) and observing them with the Asiago Astrophysical Observatory in order to derive their central  $\sigma_\star$ .

The paper is organized as follows. We derive the bulge effective radius  $r_e$  from the analysis of broad-band imaging in Section 2. We measure the central stellar velocity dispersion from ground-based spectroscopy and apply the aperture correction to  $r_e/8$  in Section 3. We obtain the dis-

\* Based on observations with the Hubble Space Telescope (HST) obtained at Space Telescope Science Institute (STScI), which is operated by the Association of Universities for Research in Astronomy (AURA), Inc., under National Aeronautics and Space Administration (NASA) contract NAS5-26555.

\*\* Corresponding author: [ilaria.pagotto@phd.unipd.it](mailto:ilaria.pagotto@phd.unipd.it)

**Table 1** Properties of the galaxy sample.

Galaxy	Mor. T.	Bar	Sp. Cl.	$D$ [Mpc]	$M_B^0$ [mag]	$\sigma_c$ [km s <sup>-1</sup> ]	$\sigma_e$ [km s <sup>-1</sup> ]	$M_\bullet$ [33°] [M <sub>⊙</sub> ]	$M_\bullet$ [81°] [M <sub>⊙</sub> ]
(1)	(2)	(3)	(4)	(5)	(6)	(7)	(8)	(9)	(10)
NGC 2654	SBab: sp	yes	-	19.4	-19.77	150 ± 3	162 ± 3	1.9e7	4.2e6
NGC 3049	SB(rs)ab	yes	H	23.9	-19.12	84 ± 9	86 ± 10	4.3e6	1.2e6
NGC 3259	SAB(rs)bc:	no	S1	24.0	-19.40	76 ± 7	63 ± 6	3.6e6	1.0e6
NGC 4343	SA(rs)b:	no	-	18.1	-18.92	110 ± 4	154 ± 5	6.4e7	5.1e7
NGC 5141	S0	-	-	72.4	-20.59	248 ± 7	222 ± 6	6.3e8	2.0e8
NGC 5635	S pec	no	-	60.1	-20.96	238 ± 6	216 ± 5	1.1e9	2.9e8
NGC 5713	SAB(rs)bc pec	yes	H	28.3	-20.68	71 ± 5	78 ± 6	3.4e7	1.4e7

*Notes.* Col.(1): galaxy name. Col.(2): morphological type from de Vaucouleurs et al. (1991, RC3). Col.(3): presence of the bar according to the photometric decomposition. We inferred the presence of a bar in the edge-on galaxy NGC 2654 from its boxy/peanut bulge. NGC 5141 turned out to be an elliptical galaxy. Col.(4): nuclear spectral class from NED, where H = HII nucleus, L = LINER, S1 = Seyfert of type 1. Col.(5): distance. The distances were obtained as  $D = V_{3K}/H_0$ , where  $V_{3K}$  is the weighted mean recessional velocity corrected to the reference frame of the microwave background radiation given in RC3 and adopting  $H_0 = 75 \text{ km s}^{-1} \text{ Mpc}^{-1}$ . Col.(6): absolute total corrected  $B$  magnitude obtained from  $B_T^0$  (RC3) and adopted distance. Col.(7): stellar velocity dispersion within  $r_e/8$  from this paper. Col.(8): stellar effective velocity dispersion within circularized  $r_e$  from the aperture correction from Falcón-Barroso et al. (2017). Col.(9): stringent  $M_\bullet$  limit assuming  $i = 33^\circ$  for the gas disk from this paper. Col.(10): stringent  $M_\bullet$  limit assuming  $i = 81^\circ$  for the gas disk from this paper.

tribution and central velocity dispersion of the ionized gas from HST spectroscopy in Section 4. We estimate the stringent  $M_\bullet$  limit from gas dynamics in Section 5. Finally, we discuss our results in the framework of the  $M_\bullet - \sigma_\star$  relation in Section 6. In this work we adopt  $H_0 = 75 \text{ km s}^{-1} \text{ Mpc}^{-1}$ ,  $\Omega_M = 0.3$ , and  $\Omega_\Lambda = 0.7$  as cosmological parameters.

## 2 Surface-brightness distribution

### 2.1 Sloan Digital Sky Survey imaging

We retrieved the flux-calibrated  $i$ -band images of the sample galaxies from the Data Release 12 of the Sloan Digital Sky Survey (SDSS-DR12, Alam et al. 2015).

We measured the sky level to be subtracted from the image of each sample galaxy, as done in Morelli et al. (2016). We masked the stars, galaxies, and spurious sources in the galaxy neighborhoods and measured its surface brightness radial profile with the ELLIPSE task in IRAF<sup>1</sup>. First, we fitted the galaxy isophotes with ellipses having the center, ellipticity, and position angle free to vary. Then, we repeated the isophotal fit fixing the center we previously obtained for the inner ellipses and the ellipticity and position angle of the outer ones. We calculated the sky level by averaging the surface brightness measured at large radii, where there is no light contribution from the galaxy. We used the IRAF task IMEXAMINE to measure the standard deviation of the background in the sky-subtracted images and to fit the stars of the field of view with a circular Moffat profile (Moffat 1969), which we adopted to model the point spread function (PSF). Finally, we trimmed the sky-subtracted images to reduce the computing time required to perform a reliable photometric decomposition and we ran ELLIPSE on

the trimmed images to derive the radial profiles of surface brightness, ellipticity, and position angle. They were used as an input to get the starting guesses of the galaxy structural parameters for the two-dimensional photometric decomposition.

### 2.2 Photometric decomposition

To measure the effective radius of the bulge, we performed the two-dimensional photometric decomposition of the SDSS images of the sample galaxies by using the Galaxy Surface Photometry 2-Dimensional Decomposition algorithm (GASP2D, Méndez-Abreu et al. 2008, 2014).

GASP2D performs a two-dimensional parametric photometric decomposition assuming that the observed surface brightness of the galaxy in each image pixel is expressed as the sum of analytical functions describing the light contribution of the structural components. We modeled (1) the surface brightness of the bulge with a Sérsic law (Sérsic 1968)

$$I_{\text{bulge}}(r) = I_e 10^{-b_n [(r/r_e)^{1/n} - 1]}, \quad (1)$$

where  $r_e$  is the effective radius,  $I_e$  is the surface brightness at  $r_e$ ,  $n$  is the shape parameter of the surface brightness profile, and  $b_n = 0.868n - 0.142$  (Caon et al. 1993) is a normalization coefficient; (2) the surface brightness of the disk either with a single exponential law (Freeman 1970)

$$I_{\text{disk}}(r) = I_0 e^{-r/h}, \quad (2)$$

where  $I_0$  is the central surface brightness and  $h$  is the scale-length, or with a double-exponential law (van der Kruit 1979)

$$I_{\text{disk}}(r) = I_0 e^{-r_{\text{break}}(h_{\text{out}} - h)/(h_{\text{out}} h)} e^{-r/h}, \quad (3)$$

where  $I_0$  is the central surface brightness,  $r_{\text{break}}$  is the break radius at which the slope change occurs,  $h$  and  $h_{\text{out}}$  are the

<sup>1</sup> Image Reduction and Analysis Facility is distributed by the National Optical Astronomy Observatory (NOAO), which is operated by the AURA, Inc., under cooperative agreement with the National Science Foundation.

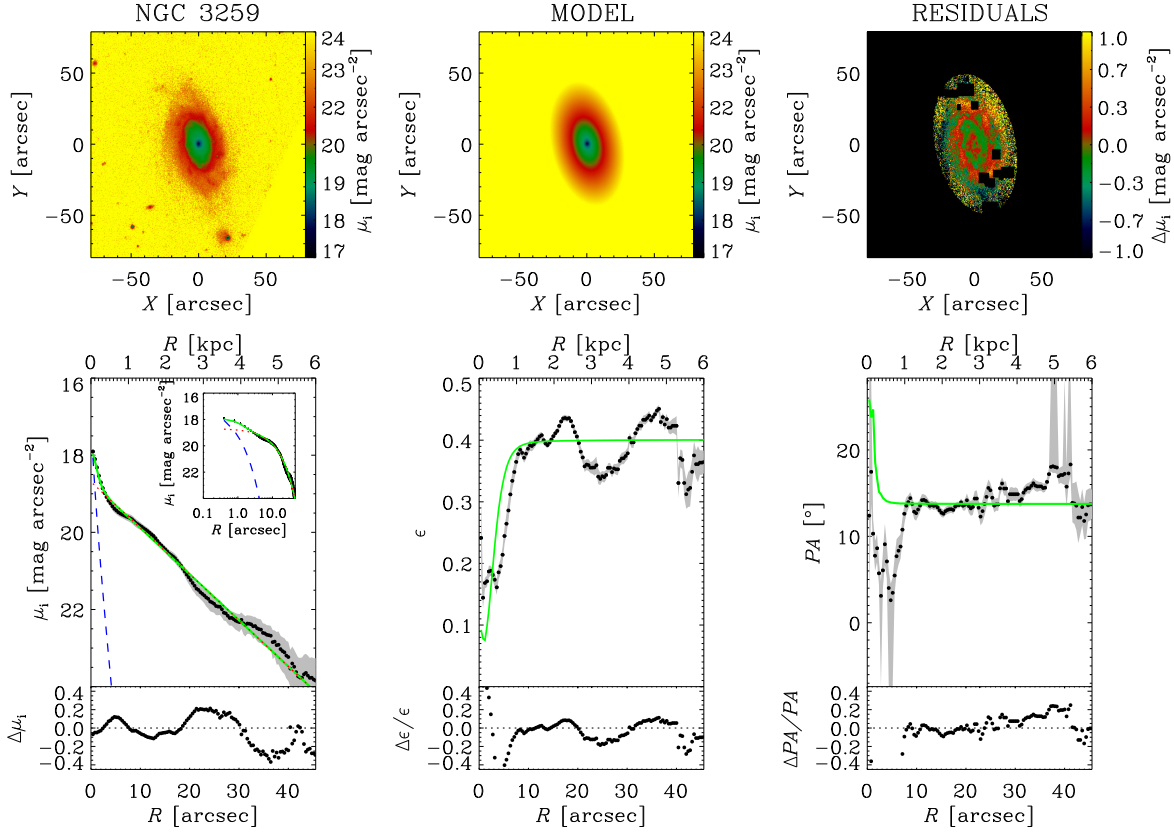


**Fig. 1** Two-dimensional photometric decomposition of the *i*-band SDSS image of NGC 3259. The images in the upper panels are oriented with the North up and the East left. *Top left panel*: map of the observed surface-brightness distribution. *Top middle panel*: map of the modeled surface-brightness distribution. *Top right panel*: map of the residuals obtained by subtracting the modeled from the observed surface-brightness distribution. The black areas are not considered in the fit. *Bottom left panel*: ellipse-averaged radial profile of the surface brightness extracted from the observed (black dots with gray error bars) and modeled image (green solid line). The intrinsic profiles of the bulge (blue dashed line) and disk (red dotted line) are shown in linear and logarithmic radial scale (*upper inset*). *Bottom middle panel*: ellipse-averaged radial profile of the ellipticity extracted from the observed (black dots with gray error bars) and modeled image (green solid line). *Bottom right panel*: ellipse-averaged radial profile of the position angle extracted from the observed (black dots with gray error bars) and modeled image (green solid line). The comparison between the ellipse-averaged profiles of the observed and model images shows the quality of the decomposition.

scaleglengths of the inner and outer exponential profiles, respectively; (3) the surface brightness of the bar with a Ferrers law (Ferrers 1877; Aguerri et al. 2009)

$$I_{\text{bar}}(r) = \begin{cases} I_{0,\text{bar}} \left[ 1 - \left( r/a_{\text{bar}} \right)^2 \right]^{2.5} & \text{if } r \leq a_{\text{bar}} \\ 0 & \text{if } r > a_{\text{bar}}, \end{cases} \quad (4)$$

where  $I_{0,\text{bar}}$  is the central surface brightness and  $a_{\text{bar}}$  is the bar length. We assumed the isophotes of the bulge, disk, and bar to be elliptical, centered onto the galaxy center, and with constant position angle  $PA_{\text{bulge}}$ ,  $PA_{\text{disk}}$ , and  $PA_{\text{bar}}$  and constant axial ratio  $q_{\text{bulge}}$ ,  $q_{\text{disk}}$ , and  $q_{\text{bar}}$ , respectively. We did not considered other components, such as rings, lenses, ovals, or spiral arms.

GASP2D returns the best-fitting values of the structural parameters of the bulge ( $I_e$ ,  $r_e$ ,  $n$ ,  $PA_{\text{bulge}}$ ,  $q_{\text{bulge}}$ ), disk ( $I_0$ ,

$h$ ,  $h_{\text{out}}$ ,  $r_b$ ,  $PA_{\text{disk}}$ ,  $q_{\text{disk}}$ ), and bar ( $I_{0,\text{bar}}$ ,  $a_{\text{bar}}$ ,  $PA_{\text{bar}}$ ,  $q_{\text{bar}}$ ) with a  $\chi^2$  minimization by weighting the surface brightness of the image pixels according to the variance of the total observed photon counts due to the contribution of both galaxy and sky. It accounts as well for photon noise, CCD gain and read-out noise, and image PSF. We derived the errors on the structural parameters by analyzing a sample of mock galaxies generated with Monte Carlo simulations, as done by Costantin et al. (2017).

We successfully performed the photometric decomposition of all the sample galaxies, except for NGC 2654, NGC 4343, and NGC 5635. For the barred galaxy NGC 3049, we adopted the double-exponential disk to fit the slope change measured in the surface brightness distribution at about 50 arcsec. We fitted NGC 3259 with a Sérsic bulge and an exponential disk, although it is classi-

**Table 2** Structural parameters of the sample galaxies from the photometric decomposition of the *i*-band SDSS images.

Parameter (1)	NGC 3049 (2)	NGC 3259 (3)	NGC 5141 (4)	NGC 5713 (5)
$\mu_e$ [mag arcsec <sup>-2</sup> ]	19.4 ± 0.8	19.4 ± 0.6	21.25 ± 0.07	19.8 ± 0.4
$r_e$ [arcsec]	5.2 ± 0.1	1.06 ± 0.02	18.0 ± 0.2	8.7 ± 0.2
$n$	0.97 ± 0.02	1.28 ± 0.01	5.58 ± 0.03	1.93 ± 0.02
$q_{\text{bulge}}$	0.270 ± 0.006	1.000 ± 0.003	0.704 ± 0.001	0.311 ± 0.005
$PA_{\text{bulge}}$ [°]	35.8 ± 0.9	13.8 ± 0.5	74.3 ± 0.1	115.1 ± 0.5
$\mu_0$ [mag arcsec <sup>-2</sup> ]	21.64 ± 0.03	18.7 ± 0.6	-	19.6 ± 0.1
$h$ [arcsec]	64.1 ± 0.6	9.1 ± 0.1	-	22.0 ± 0.1
$h_{\text{out}}$ [arcsec]	16.0 ± 0.3	-	-	-
$r_{\text{break}}$ [arcsec]	47.4 ± 0.7	-	-	-
$q_{\text{disk}}$	0.596 ± 0.002	0.599 ± 0.002	-	0.916 ± 0.001
$PA_{\text{disk}}$ [°]	27.36 ± 0.09	13.7 ± 0.2	-	33.15 ± 0.05
$\mu_{0,\text{bar}}$ [mag arcsec <sup>-2</sup> ]	20.97 ± 0.03	-	-	19.91 ± 0.04
$a_{\text{bar}}$ [arcsec]	60.8 ± 0.2	-	-	40.05 ± 0.07
$q_{\text{bar}}$	0.182 ± 0.001	-	-	0.549 ± 0.001
$PA_{\text{bar}}$ [°]	29.74 ± 0.06	-	-	98.73 ± 0.03
$L_{\text{bulge}}/L_T$	0.11	0.03	1.00	0.08
$L_{\text{disk}}/L_T$	0.71	0.97	-	0.76
$L_{\text{bar}}/L_T$	0.18	-	-	0.16

Notes.  $L_{\text{bulge}}/L_T$ ,  $L_{\text{disk}}/L_T$ , and  $L_{\text{bar}}/L_T$  are the bulge-to-total, disk-to-total, and bar-to-total luminosity ratio, respectively.

fied as a weakly barred galaxy. Indeed, an accurate inspection of the image shows that what it looks like a bar is actually an artifact resulting from the tightly wound spiral arms. NGC 5141 is classified as a lenticular galaxy, but we successfully fitted its surface brightness with a single Sérsic component. The best-fitting model was chosen by applying the Bayesian information criterion (Schwarz 1978) as done in Méndez-Abreu et al. (2017a,b) to discriminate between ellipticals and lenticulars. Therefore, the best-fitting value of  $r_e$  refers to the entire galaxy. The prominent spiral arms of NGC 5713 produce the abrupt changes in surface brightness, ellipticity, and position angles measured at about 30 arcsec. We included the bar component in the fit in order to not overestimate the bulge contribution. We show in Fig. 1 the photometric decomposition of NGC 3259 as an example and report the results for the sample galaxies we analyzed in Table 2. We present in Fig. A1 the photometric decompositions of the remaining sample galaxies.

The GASP2D photometric decomposition of the *i*-band SDSS image of NGC 5635 was performed by Méndez-Abreu et al. (2017a) and we took for the bulge their best-fitting value of  $r_e = 8.0 \pm 0.9$  arcsec.

NGC 2654 and NGC 4343 are two nearly edge-on galaxies. This prevented us from performing the photometric decomposition with GASP2D, which is best designed for galaxies with low-to-intermediate inclination (see Méndez-Abreu et al. 2008, for a discussion). We adopted the bulge  $r_e$  obtained by Salo et al. (2015, NGC 2654:  $r_e = 3.9$  arcsec, NGC 4343:  $r_e = 18.7$  arcsec) from the analysis of the infrared images of the Spitzer Survey of Stellar Structure in Galaxies (S<sup>4</sup>G, Sheth et al. 2010).

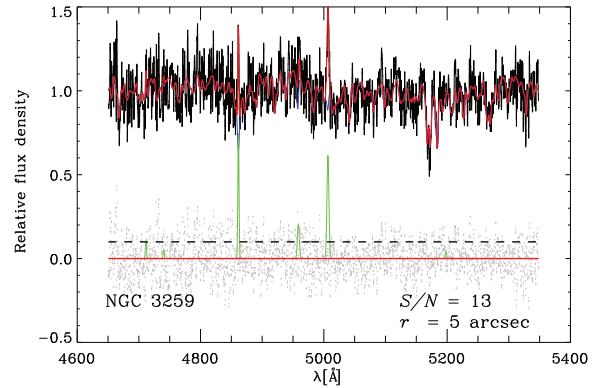


**Fig. 2** Rest-frame T122/B&C spectrum of NGC 3259 (black solid line) with the best-fitting model (red solid line) that is calculated as the sum of the spectra of the ionized-gas (green solid line) and stellar (blue solid line) components. The residuals (gray points) are defined as the difference between the observed and model spectrum. The  $S/N$  is provided per resolution element and  $r$  gives the size of the central aperture where we extracted the spectrum and measured  $\sigma_*$ .

## 3 Stellar kinematics

### 3.1 Ground-based spectroscopy

We performed the spectroscopic observations of the sample galaxies from 2016 January 4 to May 5 with the 1.22-m Galileo telescope (T122) at the Asiago Astrophysical Observatory (Italy). We used the Boller & Chivens spectrograph (B&C) and the grating with 1200 grooves mm<sup>-1</sup> in combination with a 2 arcsec × 7.75 arcmin slit and the Andor iDus DU440 CCD composed by 2048 × 512 pixels of 26 μm × 26 μm each. The CCD gain and readout

**Table 3** Details of the T122/B&C observations and central stellar velocity dispersion of the sample galaxies.

Galaxy (1)	<i>PA</i>	Exp. T. [h]	Apert.		$\sigma_{\star}$ [km s <sup>-1</sup> ] (6)
	[°] (2)		[arcsec] (4)	[pc] (5)	
NGC 2654	63	3.0	3 × 2	282 × 188	144 ± 3
NGC 3049	25	5.0	5 × 2	579 × 232	81 ± 9
NGC 3259	20	3.5	5 × 2	581 × 233	68 ± 6
NGC 4343	133	3.0	3 × 2	263 × 175	112 ± 4
NGC 5141	80	3.0	3 × 2	1053 × 702	253 ± 7
NGC 5635	65	3.5	3 × 2	874 × 583	235 ± 6
NGC 5713	10	3.0	3 × 2	412 × 274	70 ± 5

*Notes.* Col.(1): galaxy name. Col.(2): position angle of the slit along the galaxy major axis as given by RC3. Col.(3): total exposure time. Col.(4): size of the central aperture where we measured the stellar velocity dispersion. Col.(5): physical size of the central aperture where we measured the stellar velocity dispersion. Col.(6): central stellar velocity dispersion.

noise rms were  $0.97 e^{-} \text{ADU}^{-1}$  and  $3.4 e^{-}$ , respectively. The spectra were characterized by a wavelength range between about 4500–5700 Å with a reciprocal dispersion of  $0.60 \text{ \AA pixel}^{-1}$  and a spatial scale of  $1.0 \text{ arcsec pixel}^{-1}$ . We estimated the instrumental resolution as the mean of the Gaussian FWHMs measured for the unblended emission lines of a wavelength-calibrated comparison spectrum. We found  $FWHM_{\text{inst}} = 1.578 \pm 0.002 \text{ \AA}$  corresponding to  $\sigma_{\text{inst}} \simeq 40 \text{ km s}^{-1}$  at 5100 Å. During the observing nights, we measured a seeing  $FWHM_{\text{PSF}} = 3\text{--}5 \text{ arcsec}$  by fitting the guiding star with a circular Gaussian function.

We observed all the sample galaxies by centering their nucleus into the slit which we aligned along the galaxy major axis according to the position angle tabulated in Table 3. We splitted the total integration time into single exposures of 1800 s each for a better rejection of cosmic ray events. At the beginning of each exposure, we moved the slit of 10 arcsec along the galaxy major axis in order to avoid that bad pixels occurred in the same CCD position. During each night, we observed some spectrophotometric standard stars from the list of Hamuy et al. (1992, 1994) to successfully perform the flux calibration. Finally, we obtained a comparison spectrum of the available HeFeAr arc lamp before and after each object exposure to ensure an accurate wavelength calibration. The total exposure time of the T122 spectra is reported in Table 3.

We reduced the T122 spectra using standard tasks in IRAF, as done in Corsini et al. (2017). The reduction steps included the subtraction of bias, correction for internal and sky flat-field, trimming of the spectra, removal of bad pixels and cosmic rays, correction for CCD misalignment, subtraction of the sky contribution, wavelength and flux calibration, alignment, and combination of the spectra obtained for the same galaxy. The combined T122 spectrum of NGC 3259 is given in Fig. 2. The T122 spectra of the remaining sample galaxies are presented in Fig. A2.

### 3.2 Absorption-line fitting

To measure the central stellar velocity dispersion, we analyzed the absorption lines in the combined T122 spectra of the sample galaxies with the Penalized Pixel Fitting (pPXF, Cappellari & Emsellem 2004) and Gas and Absorption Line Fitting (GANDALF, Sarzi et al. 2006) algorithms.

For each galaxy, we rebinned the combined spectrum along the dispersion direction to a logarithmic scale and we deredshifted it to rest frame. Then, we averaged the rebinned spectrum along the spatial direction either to cover a nearly square aperture (Table 3) or to have a signal-to-noise ratio  $S/N \geq 10$  per resolution element. We convolved a linear combination of stellar spectra from the ELODIE library at medium resolution ( $\sigma_{\text{inst}} = 13 \text{ km s}^{-1}$ , Prugniel & Soubiran 2001) with a Gauss-Hermite line-of-sight velocity distribution (LOSVD, Gerhard 1993; van der Marel & Franx 1993) to fit the summed spectrum by a  $\chi^2$  minimization in pixel space. We selected 229 stellar spectra to fully cover the ELODIE parameter space of the effective temperature, surface gravity, and metallicity. They were broadened to match the T122 instrumental resolution, logarithmically rebinned, and cropped along the dispersion direction in order to match the wavelength range of each galaxy spectrum.

In addition, we simultaneously fitted all the ionized-gas emission lines in the covered wavelength range. We also added a fourth-order multiplicative Legendre polynomial to correct for reddening and large-scale residuals of flat-fielding. We excluded from the fitting procedure the wavelength ranges with a spurious signal coming from imperfect subtraction of cosmic rays and sky emission lines.

First, we obtained the best-fitting values of the LOS velocity  $v_{\star}$ , velocity dispersion  $\sigma_{\star}$ , and Gauss-Hermite coefficients  $h_3$  and  $h_4$  of the stellar component. The fitting procedure returned the value of  $\sigma_{\star}$  corrected for instrumental resolution. After checking that  $h_3 = h_4 = 0$  within the errors, we fitted again the galaxy spectra adopting a Gaussian LOSVD to measure  $\sigma_{\star}$  (Table 3). We assumed its error to be the formal error of the best fit after evaluating  $\chi^2$  to achieve  $\chi^2 = N_{\text{dof}} = N_{\text{d}} - N_{\text{fp}}$ , where  $N_{\text{dof}}$ ,  $N_{\text{d}}$ , and  $N_{\text{fp}}$  are the number of the degrees of freedom, data points, and fitting parameters, respectively (Press et al. 1992). The best-fitting model of the T122 spectrum of NGC 3259 is displayed in Fig. 2. Finally, for full consistency with Beifiori et al. (2009, 2012) we applied the aperture correction of Jørgensen et al. (1995) to obtain the stellar velocity dispersion  $\sigma_{\text{c}}$ , that would have been measured within a circular aperture of radius  $r_{\text{c}}/8$  (Table 1).

## 4 Ionized-gas distribution and kinematics

### 4.1 Hubble Space Telescope spectroscopy

From the Hubble Data Archive, we retrieved the STIS spectra of the sample galaxies obtained with the G750M grating through either the  $0.1 \times 52 \text{ arcsec}^2$  or the  $0.2 \times 52 \text{ arcsec}^2$  slit placed across the galaxy nucleus at position angle close

**Table 4** Details of the HST/STIS observations and central gas velocity dispersion of the sample galaxies.

Galaxy	Prop. Id.	PA [°]	Exp. T. [h]	Sp. Range [Å]	Slit [arcsec]	Bin.	Apert.		$\sigma_{\text{gas}}$ [km s <sup>-1</sup> ]
(1)	(2)	(3)	(4)	(5)	(6)	(7)	[arcsec]	[pc]	(10)
NGC 2654	9046	62.0	1.25	6480–7060	0.1	1 × 1	0.15 × 0.1	14 × 9	71 ± 13
NGC 3049	7513	42.1	0.27	6300–6870	0.1	1 × 1	0.15 × 0.1	17 × 12	31 ± 2
NGC 3259	8228	20.1	0.24	6480–7060	0.2	1 × 1	0.25 × 0.2	29 × 23	23 ± 3
NGC 4343	9068	144.1	0.81	6300–6870	0.2	1 × 1	0.25 × 0.2	22 × 18	79 ± 15
NGC 5141	8236	72.3	0.36	6480–7060	0.2	2 × 2	0.30 × 0.2	105 × 70	142 ± 6
NGC 5635	7354	63.6	0.13	6480–7060	0.1	2 × 1	0.15 × 0.1	44 × 29	333 ± 25
NGC 5713	8228	10.1	0.20	6480–7060	0.2	2 × 2	0.30 × 0.2	41 × 27	49 ± 6

*Notes.* Col.(1): galaxy name. Col.(2): HST proposal number. Col.(3): position angle of the slit. Col.(4): total exposure time. Col.(5): spectral range. Col.(6): size of the slit. Col.(7): pixel binning. Col.(8): size of the central aperture where the gas velocity dispersion was measured. Col.(9): physical size of the central aperture where the gas velocity dispersion was measured. Col.(10): central gas velocity dispersion.

to the galaxy major axis. The detector was a SITe CCD with  $1024 \times 1024$  pixel of  $21 \times 21 \mu\text{m}^2$ . The spectra covered a wavelength range of either 6480–7060 or 6300–6870 Å, depending on the tilt angle of the grating. The reciprocal dispersion was 0.554 and 1.108 Å pixel<sup>-1</sup> for the 1-pixel and 2-pixel binning read-out mode along the dispersion direction, respectively. This setup yielded an instrumental FWHM of 0.87 Å ( $\sigma_{\text{inst}} = 17 \text{ km s}^{-1}$ ) in the case of a 0.1 arcsec-wide slit and 1.6 Å ( $\sigma_{\text{inst}} = 32 \text{ km s}^{-1}$ ) for the 0.2 arcsec-wide slit (Sarzi et al. 2002; Beifiori et al. 2009). The spatial scale was 0.0507 arcsec and 0.101 arcsec pixel<sup>-1</sup> for the 1-pixel and 2-pixel binning read-out mode along the spatial direction, respectively. The HST proposal number, slit width and position angle, pixel binning, wavelength range, and total exposure times of the HST spectra of the sample galaxies are reported in Table 4.

We reduced the HST spectra using IRAF tasks, as done in Beifiori et al. (2009). The reduction steps included the subtraction of the overscan, bias and dark contributions, correction for internal flat-field, trimming of the spectra, removal of bad pixels and cosmic rays, wavelength and flux calibration, correction for geometrical distortion, alignment and combination of the spectra obtained for the same galaxy. The combined HST spectrum of NGC 3259 is shown in Fig. 3. We present in Fig. A3 the HST spectra of the remaining sample galaxies.

## 4.2 Emission-line fitting

To measure the distribution and kinematics of the ionized gas, we analyzed the [N II]λλ6548, 6583, Hα, and [S II]λλ6716, 6731 emission lines in the combined HST spectra of the sample galaxies, following the prescriptions by Beifiori et al. (2009) and using their IDL algorithm based on MPFIT package (Markwardt 2009).

We fitted the stellar continuum with a low-order polynomial and the narrow and broad components of the observed emission lines with a sum of Gaussian functions. For all the objects the ionized-gas emission was always much stronger compared to the stellar continuum. The best-fitting parameters and their errors were derived by a  $\chi^2$

minimization in pixel space and evaluating  $\chi^2 = N_{\text{dof}}$ . We adopted both a narrow and broad component for the emission lines of NGC 3259 and NGC 5141, two narrow components for NGC 3049, and a single narrow component for all the other sample galaxies, including NGC 5635 for which the presence of two distinct components was not clear. For NGC 2654 and NGC 3049 the Hα line was not accurately fitted due to the low  $S/N$  and presence of an asymmetric broad component, respectively. This does not influence our results since we considered only the [N II]λ6583 line for the dynamical modeling.

We focused on the [N II]λ6583 line because it was always the brightest nebular line in our spectra. The nebular lines actually probe the nuclear kinematics better than the Hα line, which could be affected by both the absorption from the stellar component and emission from circumnuclear starforming regions (e.g., Coccato et al. 2006).

We measured the radial profile of the [N II]λ6583 flux along the spatial direction to constrain the distribution of the ionized gas. We assumed the gas to be distributed into a infinitesimally thin disk centered on the galaxy nucleus with an intrinsically Gaussian flux profile. We derived the intrinsic flux profile for two inclinations of the gaseous disk ( $i = 33^\circ, 81^\circ$ ) by a  $\chi^2$  minimization to match the observed flux, while accounting for the STIS PSF, which we generated with the TINY TIM package by Krist et al. (2011). The result for NGC 3259 is plotted in Fig. 3. We measured the [N II]λ6583 line width within a nearly square aperture centered on the continuum peak to estimate the central gas velocity dispersion  $\sigma_{\text{gas}}$ . In the case of the 1-pixel spatial binning, we considered an aperture of 0.15 arcsec (3 pixels) or 0.25 arcsec (5 pixels) along the spatial direction when the spectrum was obtained with a 0.1 arcsec or a 0.2 arcsec-wide slit, respectively. In the case of a 2-pixel spatial binning, we took an aperture of 0.30 arcsec (3 pixels). The aperture sizes are listed in Table 4. We corrected the measured line width for instrumental resolution to obtain  $\sigma_{\text{gas}}$  (Table 4).

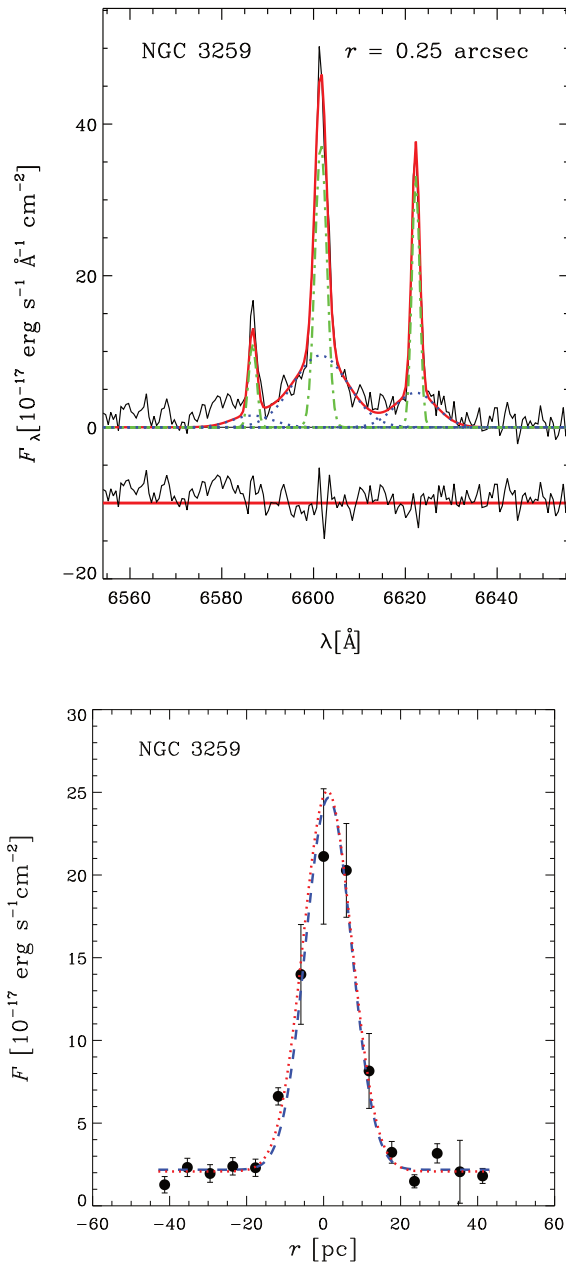


**Fig. 3** *Top panel:* HST/STIS spectrum of NGC 3259 (black solid line) with best-fitting model (red solid line) obtained adopting broad (blue dotted lines) and narrow (green dashed dotted lines) components for the  $[\text{N II}]\lambda\lambda 6548, 6583$  and  $\text{H}\alpha$  lines.  $r$  gives the size of the central aperture where we extracted the spectrum and measured  $\sigma_{\text{gas}}$ . The residuals are defined as the difference between the observed and model spectrum. They are shifted to have an arbitrary zero point for viewing convenience. *Bottom panel:* flux radial profile of the  $[\text{N II}]\lambda 6583$  emission line measured in the HST/STIS spectrum of NGC 3259. The best-fitting radial profiles of intrinsic flux for a gas disk with  $i = 33^\circ$  (blue dashed line) and  $81^\circ$  (red dotted line) are shown after being convolved with STIS PSF.

## 5 Dynamical modeling

To derive stringent  $M_\bullet$  limits for our sample galaxies we followed the approach of Sarzi et al. (2002). This is based on the assumption that the nuclear gravitational potential is traced by the line width of the nebular emission originated from ionized gas in Keplerian rotation around the SBH. We considered the gas moving onto coplanar circular orbits in a infinitesimally thin disk with the intrinsic distribution we derived from the measured flux radial profile. The kinematics was measured along only one direction across the galaxy nucleus, which does not provide constraints on the orientation of the gas disk. We disregarded the effect on the unknown position angle of the gas disk, since we extracted our spectrum in a nearly square aperture. Thus, we could assume that the STIS slit was placed along the major axis of the gas disk and we estimated  $M_\bullet$  at two inclinations of  $33^\circ$  and  $81^\circ$ , which bracket the 68% of randomly inclined disks (see Sarzi et al. 2002). Our choice of parametrization for the intrinsic flux of the gas is conservative, a cusplier function would lead to a more concentrated gas distribution and, therefore, to a smaller value of  $M_\bullet$  (see Sarzi et al. 2002). We also expect to find a smaller value of  $M_\bullet$  when taking into account the contributions of the stellar potential and non-gravitational forces (due for instance to the activity of the central SBH). These last factors imply that our  $M_\bullet$  estimates based on the assumption of a rotating gaseous disk should be strictly speaking regarded only as upper limits, although in practice it is unlikely that the gas motions are entirely driven by non-gravitational forces. In particular, the finding that the narrow-line ionized-gas emission is always rather concentrated around the nucleus contrasts with the idea that such gas would not respond to the central gravitational pull of the SBH. In fact, that non-gravitational forces are generally unimportant is also supported by the finding that the  $M_\bullet$  estimates derived from the central ionized-gas flux profile and line-width always agree with actual  $M_\bullet$  measurements based on resolved stellar and ionized-gas kinematics (Beifiori et al. 2012). Nonetheless, in some instances there are indications that  $M_\bullet$  estimates based on our method could be biased either due to the presence of non-gravitational forces or to the stellar potential (Beifiori et al. 2009).

## 6 Discussion and conclusions

In Fig. 4, we compare our stringent  $M_\bullet$  limits to those of Beifiori et al. (2009, 2012) who considered the  $M_\bullet - \sigma_c$  relation by Ferrarese & Ford (2005).

The  $M_\bullet$  limits of NGC 2654, NGC 3049, NGC 3259, NGC 4343, NGC 5141, and NGC 5635 are within the  $3\sigma$  scatter of the  $M_\bullet - \sigma_c$  relation. The  $M_\bullet$  of NGC 5635 is displaced towards higher values because we probably overestimated the  $\sigma_{\text{gas}}$  value from the HST/STIS spectrum, where it was not possible to distinguish the broad and narrow components of the  $[\text{N II}]\lambda 6583$  line. The  $M_\bullet$  value for

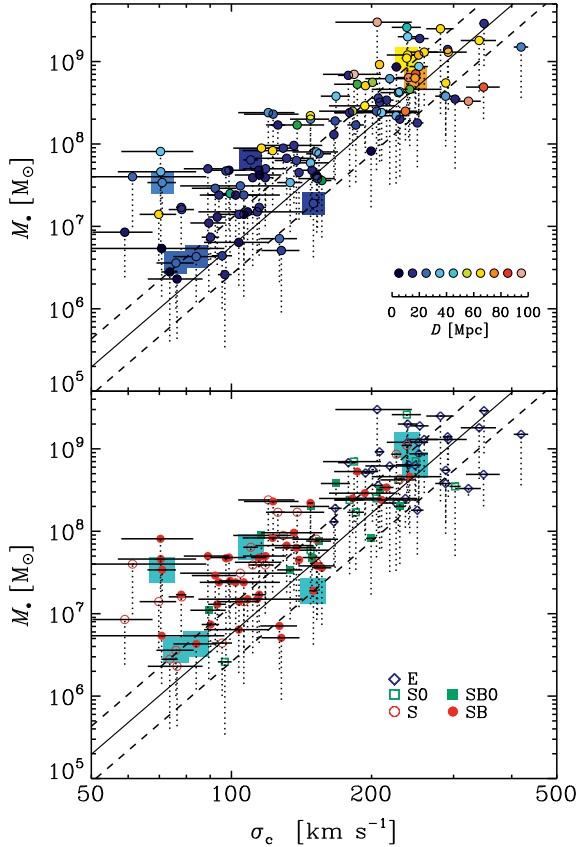


**Fig. 4** Comparison between the stringent  $M_\bullet$  limits of our (symbols with large squares) and Beifiori et al. (2009, 2012) sample of galaxies as a function of galaxy distance (*top panel*) and morphological type (*bottom panel*). The upper and lower edges of the dotted lines correspond to  $M_\bullet$  values estimated assuming an inclination of  $i = 33^\circ$  and  $81^\circ$  for the gas disk, respectively. In both panels the solid line is  $M_\bullet - \sigma_c$  relation by Ferrarese & Ford (2005) with the dashed lines showing the  $1\sigma$  (0.34 dex) scatter in  $M_\bullet$ .

NGC 5713 exceeds more than three times the scatter of the  $M_\bullet - \sigma_c$  relation. For this galaxy the contribution of the stellar mass that we disregarded in our analysis could play a significant role, as already pointed out by Beifiori et al. (2009) for a number of other galaxies with a stringent  $M_\bullet$  limit in the lower end of the  $M_\bullet - \sigma_c$  relation. On the top of this, the center of NGC 5713 is poorly constrained because its nuclear surface brightness distribution is characterized by several bright knots rather than a well defined peak (see also Scarlata et al. 2004).

Our galaxies cover different morphological types (1 elliptical, 3 unbarred and 3 barred spirals according to the photometric decomposition) and span a wide range of central stellar velocity dispersion ( $71 < \sigma_c < 248 \text{ km s}^{-1}$ ) and  $M_\bullet$  ( $3.6 \cdot 10^6 < M_\bullet < 1.1 \cdot 10^9 M_\odot$  for  $i = 33^\circ$  and  $1.0 \cdot 10^6 < M_\bullet < 2.9 \cdot 10^8 M_\odot$  for  $i = 81^\circ$ ). The stringent  $M_\bullet$  limits we measured are fully consistent with those by Beifiori et al. (2009, 2012). This is confirmed by the dis-

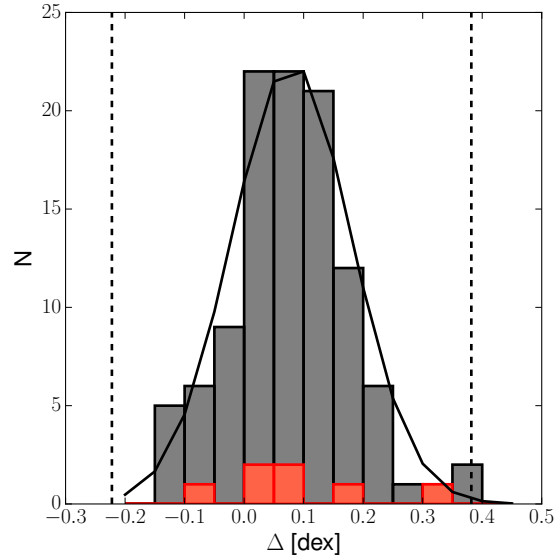


**Fig. 5** Distribution of the distance of the  $(\sigma_c, M_\bullet)$  values measured for our (red histogram) and Beifiori et al. (2009, 2012) (black histogram) sample of galaxies from the  $M_\bullet - \sigma_c$  relation by Ferrarese & Ford (2005). The black solid line is the Gaussian fit to Beifiori et al. (2009) distribution, which is centered at  $\Delta = 0.08$  dex with the black dotted lines marking its  $\pm 3\sigma$  range ( $\sigma = 0.10$  dex).

tribution of the distances of the two  $(\sigma_c, M_\bullet)$  datasets from the  $M_\bullet - \sigma_c$  relation by Ferrarese & Ford (2005), which we show in Fig. 5 for  $i = 33^\circ$ . On average, our  $M_\bullet$  run parallel and above the  $M_\bullet - \sigma_c$  relation with no systematic trend depending on the galaxy distance or presence of the bar.

With our investigation, the number of galaxies with stringent  $M_\bullet$  limits obtained from nebular-line width increases to 114 and can be used for studying the scaling relations between  $M_\bullet$  and properties of their host galaxies. Most of our  $M_\bullet$  limits actually populate the low- $\sigma$  end of the  $M_\bullet - \sigma_c$  relation. They could be used to prove the claim by Beifiori et al. (2009) that the contribution of the stellar component to the gravitational potential is particularly significant in the low- $\sigma$  regime and biases the measured  $M_\bullet$  towards exceedingly large values. This will be investigated in a forthcoming paper (Pagotto et al. in prep.) to prove previous findings suggesting that the nuclear gravitational potential is remarkably well traced by the width of the nebular lines when observed at sub-arcsecond scales.

*Acknowledgements.* We acknowledge the anonymous referee for valuable comments that led to an improved presentation. We are grateful to Heikki Salo for valuable discussion on the photometric decomposition of NGC 4343. EMC, EDB, LM, and AP are supported by Padua University through grants 60A02-5857/13, 60A02-5833/14, 60A02-4434/15, CPDA133894, and BIRD164402/16. IP acknowledges the Max-Planck-Institut für extraterrestrische Physik for the hospitality while this paper was in progress. Part of the data used in this paper were acquired through the Sloan Digital Sky Survey Archive



(<http://www.sdss.org/>). This research also made use of the HyperLeda Database (<http://leda.univ-lyon1.fr/>) and NASA/IPAC Extragalactic Database (<http://ned.ipac.caltech.edu/>).

## References

- Aguerri, J. A. L., Méndez-Abreu, J., & Corsini, E. M. 2009, *A&A*, 495, 491
- Alam, S., Albareti, F. D., Allende Prieto, C., et al. 2015, *ApJS*, 219, 12
- Beifiori, A., Sarzi, M., Corsini, E. M., et al. 2009, *ApJ*, 692, 856
- Beifiori, A., Courteau, S., Corsini, E. M., & Zhu, Y. 2012, *MNRAS*, 419, 2497
- Caon, N., Capaccioli, M., & D’Onofrio, M. 1993, *MNRAS*, 265, 1013
- Cappellari, M. & Emsellem, E. 2004, *PASP*, 116, 138
- Cocato, L., Sarzi, M., Pizzella, A., et al. 2006, *MNRAS*, 366, 1050
- Corsini, E. M., Wegner, G. A., Thomas, J., Saglia, R. P., & Bender, R. 2017, *MNRAS*, 466, 974
- Costantin, L., Méndez-Abreu, J., Corsini, E. M., et al. 2017, *A&A*, 601, 84
- de Vaucouleurs, G., de Vaucouleurs, A., Corwin, H. G., et al. 1991, *Third Reference Catalogue of Bright Galaxies* (Berlin: Springer) (RC3)
- Fabian, A.C. 1999, *MNRAS*, 308, 39
- Falcón-Barroso, J., Lyubenova, M., van de Ven, G., et al. 2017, *A&A*, 597, 48
- Ferrarese, L. & Merritt, D. 2000, *ApJ*, 539, 9
- Ferrarese, L. & Ford, H. 2005, *Space Sci. Rev.*, 116, 523
- Ferrers, N. M. 1877, *Quart. J. Pure and Appl. Math.*, 14, 1
- Freeman, K. C. 1970, *ApJ*, 160, 811
- Gebhardt, K., Bender, R., Bower, G., et al. 2000, *ApJ*, 539, 13
- Gerhard, O. E. 1993, *MNRAS*, 265, 213
- Hamuy, M., Walker, A. R., Suntzeff, N. B., et al. 1992, *PASP*, 104, 533
- Hamuy, M., Suntzeff, N. B., Heathcote, S. R., et al. 1994, 106, 566
- Jørgensen, I., Franx, M., & Kjaergaard, P. 1995, *MNRAS*, 276, 1341
- Kormendy, J. & Ho, L. C. 2013, *ARA&A*, 51, 511
- Krist, J. E., Hook, R. N., & Stoehr, F. 2011, *Proc. SPIE*, 8127, 81270J-1
- Markwardt, C. B. 2009, in *Astronomical Data Analysis Software and Systems XVIII*, eds. D. A. Bohlender, D. Durand, & P. Dowler, *ASP Conf. Ser.* 411, 251
- McConnell, N. J. & Ma, C.-P. 2013, *ApJ*, 764, 184
- Méndez-Abreu, J., Aguerri, J. A. L., Corsini, E. M., & Simonneau, E. 2008, *A&A*, 478, 353
- Méndez-Abreu, J., Debattista, V. P., Corsini, E. M., & Aguerri, J. A. L. 2014, *A&A*, 572, A25
- Méndez-Abreu, J., Ruiz-Lara, T., Sánchez-Menguiano, L., et al. 2017a, *A&A*, 598, 32
- Méndez-Abreu, J., Aguerri, J. A. L., Falcón-Barroso, J., et al. 2017b, *A&A*, submitted
- Moffat, A. F. J. 1969, *A&A*, 3, 455
- Morelli, L., Parmiggiani, M., Corsini, E. M., et al. 2016, *MNRAS*, 463, 4396
- Press, W. H., Teukolsky, S. A., Vetterling, W. T., Flannery, B. P., 1992, *Numerical Recipes in FORTRAN. The Art of Scientific Computing* (Cambridge: Cambridge Univ. Press)
- Prugniel, Ph., & Soubiran, C. 2001, *A&A*, 369, 1048
- Saglia, R. P., Opitsch, M., Erwin, P., et al. 2016, *ApJ*, 818, 47
- Salo, H., Laurikainen, E., Laine, J., et al. 2015, *ApJS*, 219, 4
- Sarzi, M., Rix, H.-W., Shields, J. C., et al. 2002, *ApJ*, 567, 237
- Sarzi, M., Falcón-Barroso, J., Davies, R. L., et al. 2006, *MNRAS*, 366, 1151
- Scarlata, C., Stiavelli, M., Hughes, M. A., et al. 2004, *AJ*, 128, 1124
- Schwarz, G. E. 1978, *Ann. Stat.*, 6, 461
- Sérsic, J. L. 1968, *Atlas de Galaxias Australes* (Cordoba: Observatorio Astronomico)
- Shankar, F., Bernardi, M., Sheth, R. K., et al. 2016, *MNRAS*, 460, 3119
- Sheth, K., Regan, M., Hinz, J. L., et al. 2010, *PASP*, 122, 1397
- Silk, J. & Rees, M. J. 1998, *A&A*, 331, 1
- van der Kruit, P. C. 1979, *A&AS*, 38, 15
- van der Marel, R. P. & Franx, M. 1993, *ApJ*, 407, 525

## A Appendix

Fig. A1, Fig. A2, and Fig. A3 show the two-dimensional photometric decomposition of the *i*-band SDSS images, the rest-frame T122/B&C spectra, and HST/STIS spectra of the sample galaxies, except for NGC 3259, respectively.

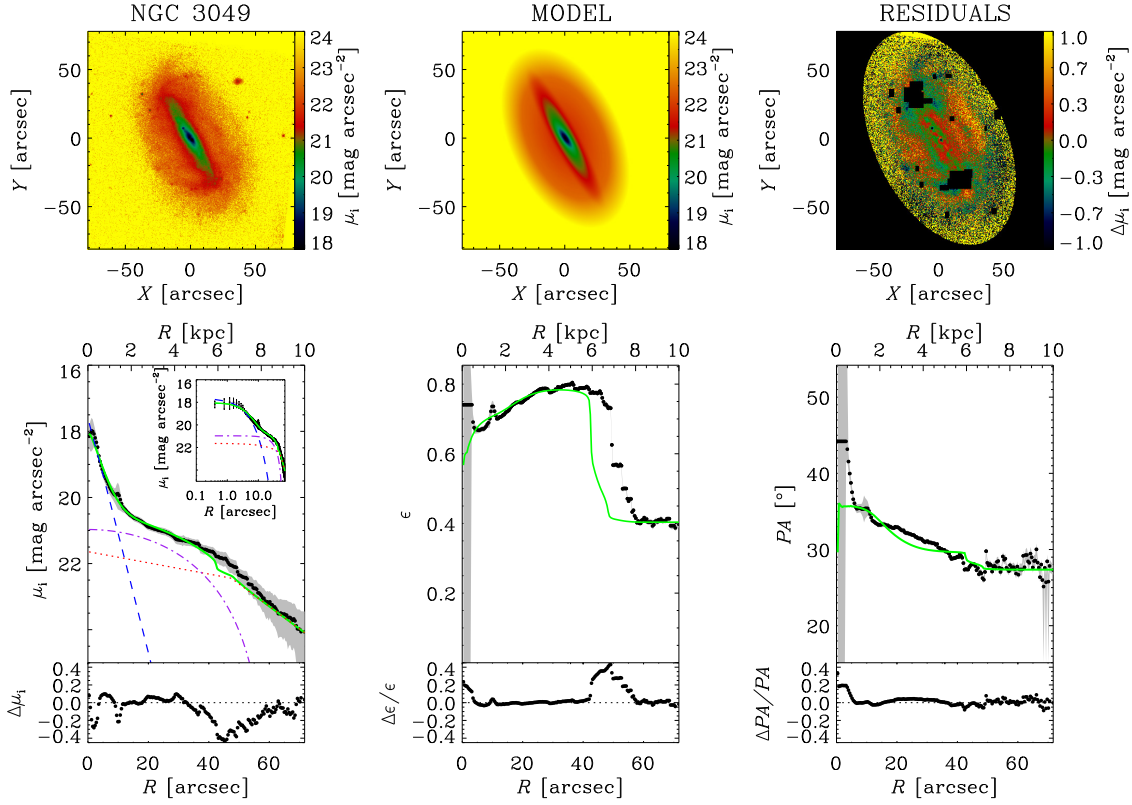


**Fig. A1** As in Fig. 1, but for the remaining sample galaxies.

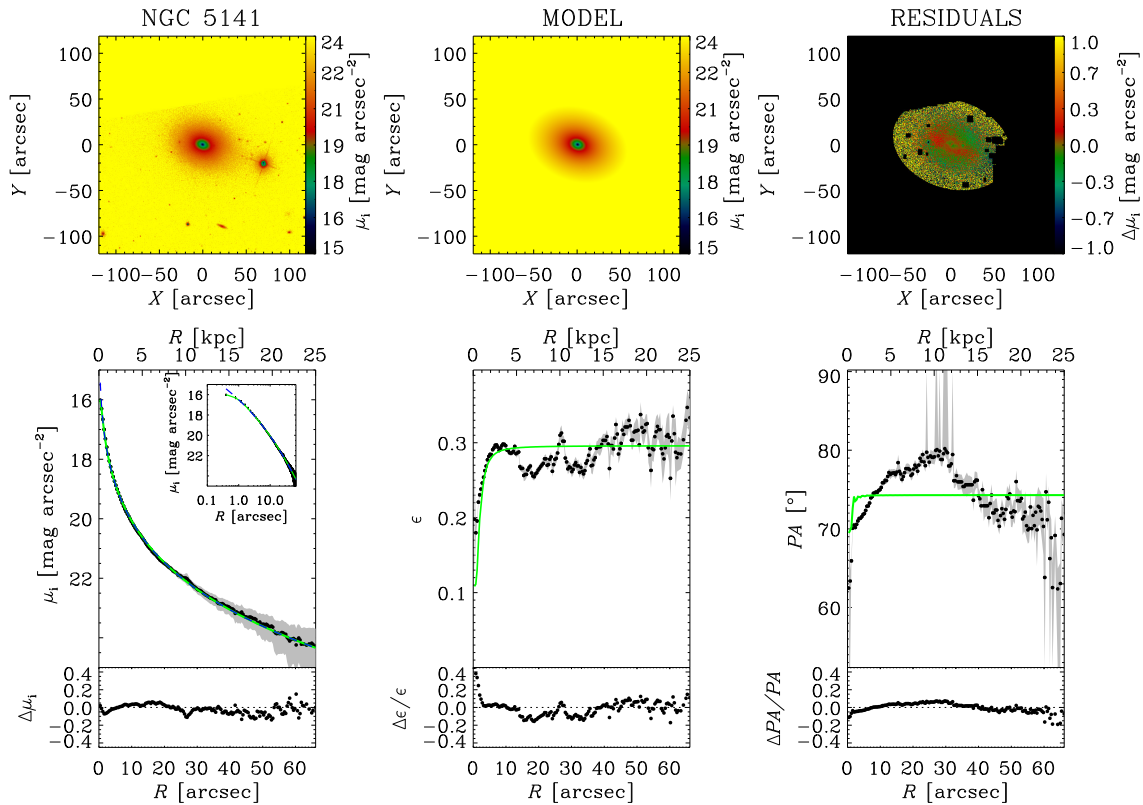


**Fig. A1** Continued.

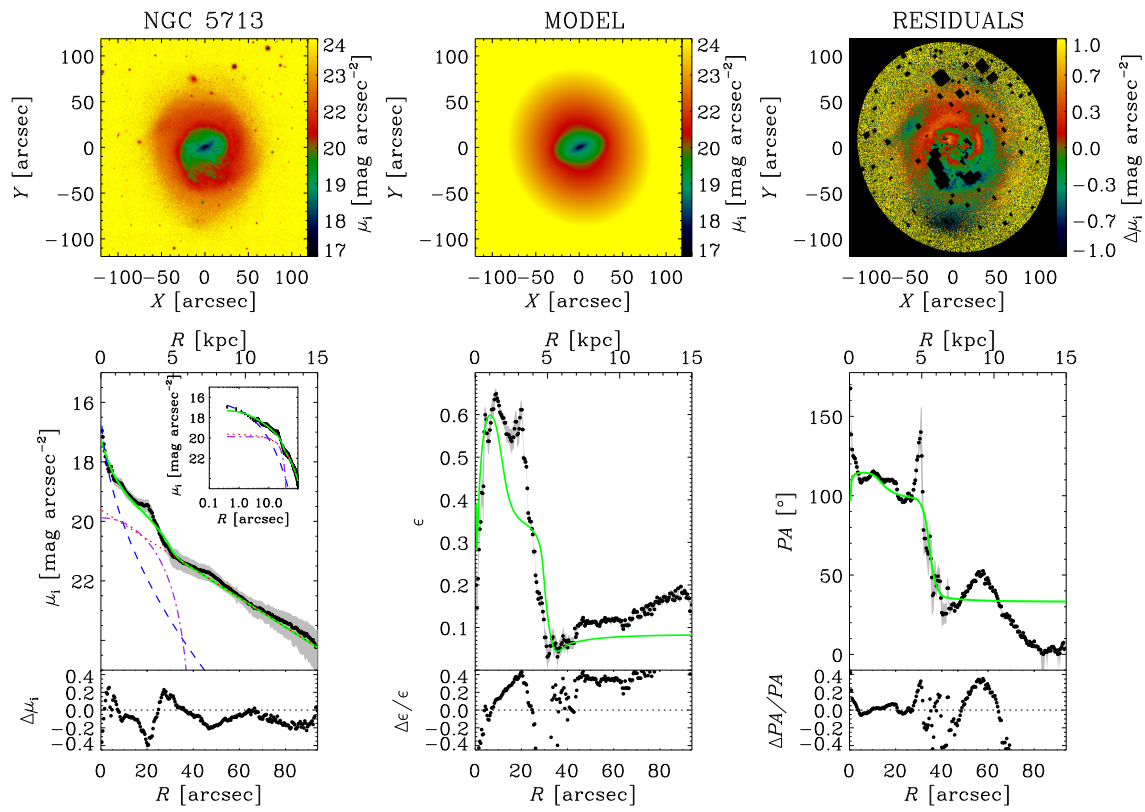
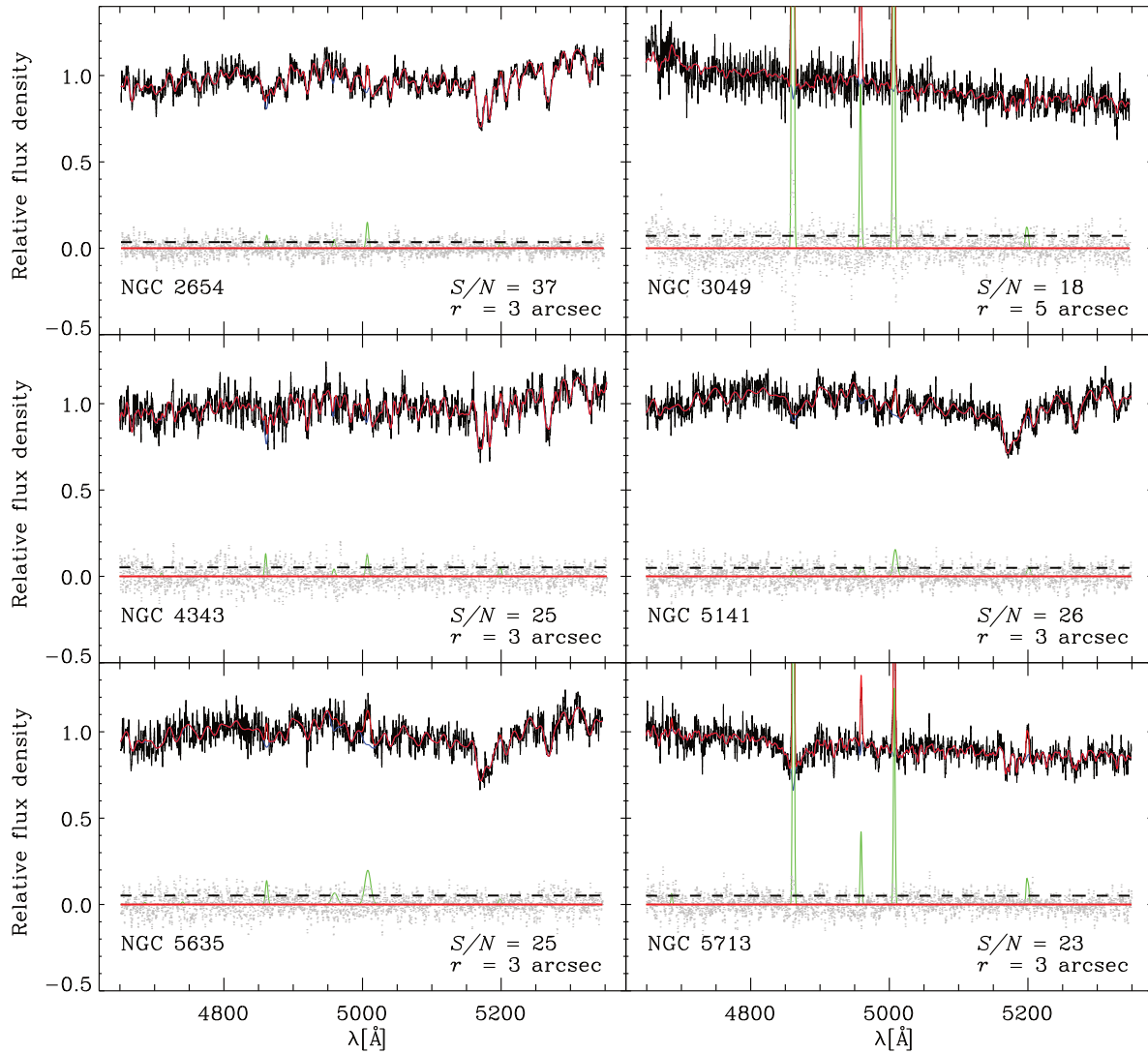
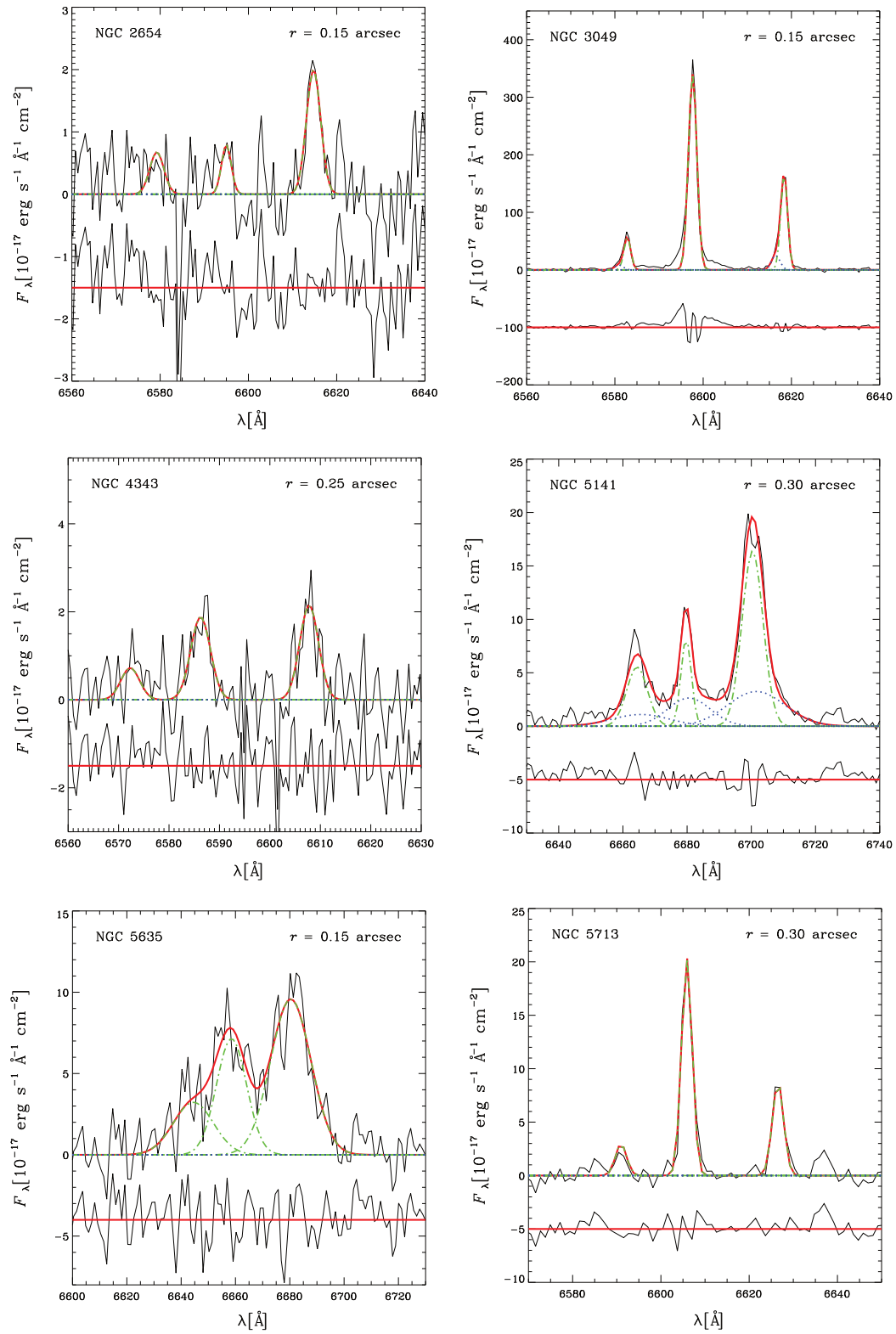


Fig. A1 Continued.



**Fig. A2** As in Fig. 2, but for the remaining sample galaxies.



**Fig. A3** As in Fig. 3, but for the remaining sample galaxies.